

Videomicroscopy, Image Processing, and Analysis of Whole Histologic Sections of the Human Brain

OLIVER SCHMITT,^{1*} REINHARD EGGERS,² AND JAN MODERSITZKI³

¹Institute of Anatomy, University of Rostock, Gertruden Str. 9, D-18055 Rostock, Germany

²Institute of Anatomy, Medical University of Lübeck, Ratzeburger Allee 160, D-23538 Lübeck, Germany

³Institute of Mathematics, Medical University of Lübeck, Wallstr. 40, D-23560 Lübeck, Germany

KEY WORDS whole brain sections; gross sections; neuroimaging; computational neuroanatomy; videomicroscopy; image analysis; image processing; neuron morphometry; neuron registration

ABSTRACT Serial histologic sections of a whole human brain may have extensions of up to 130×130 mm within the coronal plane around the temporal lobe. To date, however, technology has not provided a bright field microscope that is able to shift the object holder continuously in the x- and y-direction over such distances and still possess the same optical capabilities as comparable devices. We developed a new light microscope to continuously quantify such sections. We also developed the computing environment for controlling the device and for analyzing the data produced. In principle, we are now able to quantify each neuron of a human brain. The data ultimately will provide the most detailed structural information about the human brain ascertained thus far. Such detailed information of the spatial distribution of neurons is essential to develop realistic models for simulation of large-scale neuronal networks and to investigate the significance of neuronal arrangements with respect to neuronal signal processing in the CNS. After preprocessing of the data produced by the new microscope, we are able to detect lamination patterns in the spatial distribution of gravity centers of cells. Furthermore, morphological features like size of the projection area and mean staining intensity are visualized as a particle process. The particle process presents the sizes and staining intensity of perikaryons and allows a distinction of gray matter and white matter. These results provide evidence that the system works correctly and can be applied to a systematic analysis of a larger sequence of serial histologic sections. The objective of this study is to introduce the very large section analyzing microscope (VLSAM) and to present the initial data produced by the system. Moreover, we will discuss workload and future developments of the parallel image analysis system that are associated with the microscope. *Microsc. Res. Tech.* 66:203–218, 2005. © 2005 Wiley-Liss, Inc.

INTRODUCTION

The identification of the exact location of all neurons in a series of histologic sections is mandatory for the accurate analysis of their spatial distribution. The spatial relations of neurons seems to be optimized with regard to development processes (e.g., the myelogenesis and corticogenesis of the cerebral cortex) and to the geometry of nerve fiber pathways (Cherniak, 1992, 1994, 1995; Duijnhouwer et al., 2001; Felleman and van Essen, 1991; Mitchison, 1991; Murre and Sturdy, 1995; Young, 1992, 1996). Neurons lying closer together do exchange information in the cerebral cortex with a higher probability of speed and precision than do neurons with greater interneuronal distances (i.e., structure-function-relation, or SFR) (Ballard, 1986; Barlow, 1986; Liljas, 1999). In the past, it was unknown if the internal geometry or specific distribution, even in a massive dynamic or plastic neuronal network, determines neuronal functions between a scale of microfunctional (receptor-induced depolarization or hyperpolarization) and macrofunctional dimension (epiphenomena like behavior) (Schwartz, 1980). However, Duijnhouwer et al. (2001) have found that the electrophysiological behavior of neurons depends on the

neurons dendritic branching pattern. Thus, to study the spatial relations of neurons, it is necessary to determine their three-dimensional positions. Yet re-architecting the human brain into a three-dimensional mosaic of tissue blocks (Brodmann, 1909; von Economo and Koskinas, 1925) would involve an extreme disintegration of the neuronal tissue and thereby potentially compromise any resulting research data. The production of serial sections of a whole human brain offers a far more reliable approach. In such histologic sections, neurons can be recorded videomicroscopically and then analyzed in greater detail using morphometry by a suitable image analytic procedure. In order to produce histologic sections that can be stained with conventional methods

*Correspondence to: Oliver Schmitt, Institute of Anatomy, University of Rostock, Gertruden Str. 9, D-18055 Rostock, Germany.
E-mail: schmitt@med.uni-rostock.de

Received 6 October 2004; accepted in revised form 22 January 2005

Contract grant sponsor: Peter Dormier Foundation; Contract grant sponsor: Friedrich Bluhme Foundation; Contract grant sponsor: Else Jebsen Foundation; Contract grant sponsor: Gerhard Ten Doornkaat Koolman Foundation; Contract grant sponsor: Possehl Foundation.

DOI 10.1002/jemt.20163

Published online in Wiley InterScience (www.interscience.wiley.com).

such as cresyl violet, gallocyanin chrome alum (Schmitt and Eggers, 1997b,a), the Merker modification of the Gallyas method (Merker, 1983), or Kultschitzky, Weigert nerve fiber visualizations (Romeis, 1989), the embedding of whole brains in paraffin wax is necessary. The paraffin-brain-block then can be sectioned easily and precisely on a modified sliding microtome, the sections subsequently flattened on the surface of a warm water bath. Specially manufactured slides and coverslips are used to transfer the flattened histologic sections. The staining, especially of a series of full-size human brain sections (FIBS) (about $130 \times 130 \text{ mm}^2$), must be modified and optimized in order to produce staining results with minimal differences or inhomogeneities within the large sections to maximize all possible advantages for consecutive image analytical procedures. After all these problems are solved, next arises the challenge of how to completely scan full FIBS continuously while avoiding gaps or incongruities. A conventional motorized videomicroscope is simply too small to accommodate analysis along the traverse path of the microscope stage. True, there are light microscopes available for the inspection of wafers (Axiotron Zeiss, Polylite 88 Leica), and these microscopes may shift the FIBS continuously without apparent gaps or anomalies. However, these light microscopes all work in an episcopic mode that is not suitable for the study of transparent histologic sections. Hence, it was necessary to develop and construct a new light microscope equipped with precise videomicroscopic capability and fine-gear motorization to enable detailed analysis of coronal histologic sections of whole human brains. We describe herein the preprocessing of the biologic material, the very large section analyzing light microscope (VLSAM), and the initial results from parallel image analysis of the data generated by the VLSAM.

MATERIALS AND METHODS

Histologic Methods

The brain of a 65-year-old male without neuropathologic changes was fixed 3 months in a neutral phosphate-buffered solution of 0.9% saline and 4% formalin solution (900 ml distilled water + 4 g $\text{NaH}_2\text{PO}_4 \times \text{H}_2\text{O}$ + 6.5 g Na_2HPO_4 + 100 ml 37% formalin) at 4°C. After immersion fixation, the brain was washed for two days in running tap water. This procedure was followed by dehydration: 7 days in a first portion of fresh 80% 2-propanol, 7 days in a second portion of fresh 80% 2-propanol, 7 days in a portion of fresh 96% 2-propanol, 7 days in a second portion of fresh 96% 2-propanol, 3 days in a first portion of fresh abs. 2-propanol, 3 days in a second portion of fresh abs. 2-propanol, 3 days in a third portion of fresh abs. 2-propanol. This dehydration was followed by replacing 2-propanol with 4 fresh portions of trichloromethan lasting 7 days each. Then the brain was brought into 4 portions of paraffin for 7 days each at 60°C (Fig. 1a). This was followed by slow degassing until 15 mmHg for about 3 hours until no gas bubbles emerged out of the sulci. The paraffin wax block then was trimmed carefully and fixed on a block holder of the sliding microtome (Polycut[®], Reichert Jung) (Fig. 1a). Distance blocks for the knife holder were manufactured and installed in order to start the sectioning just above the relative high wax block (about

130 mm). All sections that had been sliced had a thickness of 20 μm . We installed a high resolution ($1,352 \times 1,795$ Pixel, 24 Bit) scanner camera (Colorscan, Schneider) equipped with a 105-mm macro lens (AF Mikro Nikko R 1:2,8D) and a special lighting device to obtain an image immediately before every sectioning (episcopic imaging) (Schormann and Zilles, 1998; Toga et al., 1994). The light tubes (Dulux L z418, Osram) generate a spectrum comparable with daylight and at a frequency (high-frequency starter EVL 238, 24 W, Eckerle) that is optimized with respect to spectral sensitivity of the scanner camera. The images produced by this device will be used in further studies to align images of deformed histologic sections to non-deformed images of the paraffin blockface.

Immediately before the paraffin wax block on the block holder was shifted against the knife (D-knife, cutting angle 0°), a color image was transmitted to a computer. After sectioning, the deformed sections (Fig. 1a) were flattened in a 40°C warm water bath. The water was degassed by boiling for more than 20 minutes to reduce small water bubbles; this was important for the subsequent staining process because the accumulation of small water bubbles between the mounted and dried sections and the slides can cause detachment. Small wrinkles and folds were removed by teasing them apart with forceps. After flattening, each section was maneuvered very carefully on specially manufactured slides (1-mm thick; $150 \times 150 \text{ mm}$, Menzel). The slides were degreased in absolute ethanol and then coated with an adhesive solution of 5 g gelatine + 0.5 g $\text{KCr}(\text{SO}_4)_2 \times 12 \text{ H}_2\text{O}$ (chrome alum) + 1,000 ml aqua bidest. The sections were blotted lightly with moistened blotting paper to remove excess water and to increase contact between section and slide. We dried the prepared sections for at least 24 hours at 37°C, letting us then deparaffin the sections in 3 portions of xylene followed by a descending series of 2-propanols. This procedure was followed by staining in gallocyanin chrome alum (Fig. 2) because it is a perikaryon staining that also reacts with RNA and DNA. It provides optimal homogeneous staining results, e.g., no trends of the staining intensity within the section (Schmitt and Eggers, 1997a,b).

The latter effect was important for a reliable image analysis of the homogeneously stained neurons. The staining solution contained 0.5 g gallocyanin and 13 g chrome alum, which were boiled for 15 minutes in 100 ml distilled water, cooled, matured overnight (about 12 to 18 hours), and then filtered. This solution was mixed with one stock solution that consisted of 0.53 g sodiumcarbonate diluted in 100 ml distilled water and a second stock solution that contained 1.91 g sodium-tetraborate-decahydrate diluted in 100 ml distilled water. Following this procedure, 97.3 ml of stock solution one and 2.7 ml of stock solution two were mixed with 100 ml of the filtered gallocyanin chrome alum solution. Overnight pH-stabilization proved to be necessary in order to adjust the pH with 5N HCl to a stable pH of 1.65 at 37°C. The deparaffined sections then were transferred into distilled water and subsequently immersed for 5 minutes in an acidic solution (pH 1.65) to reduce background staining. After adapting the sections to a pH of 1.65, they were placed into the staining solution for 24 hours at 37°C followed by

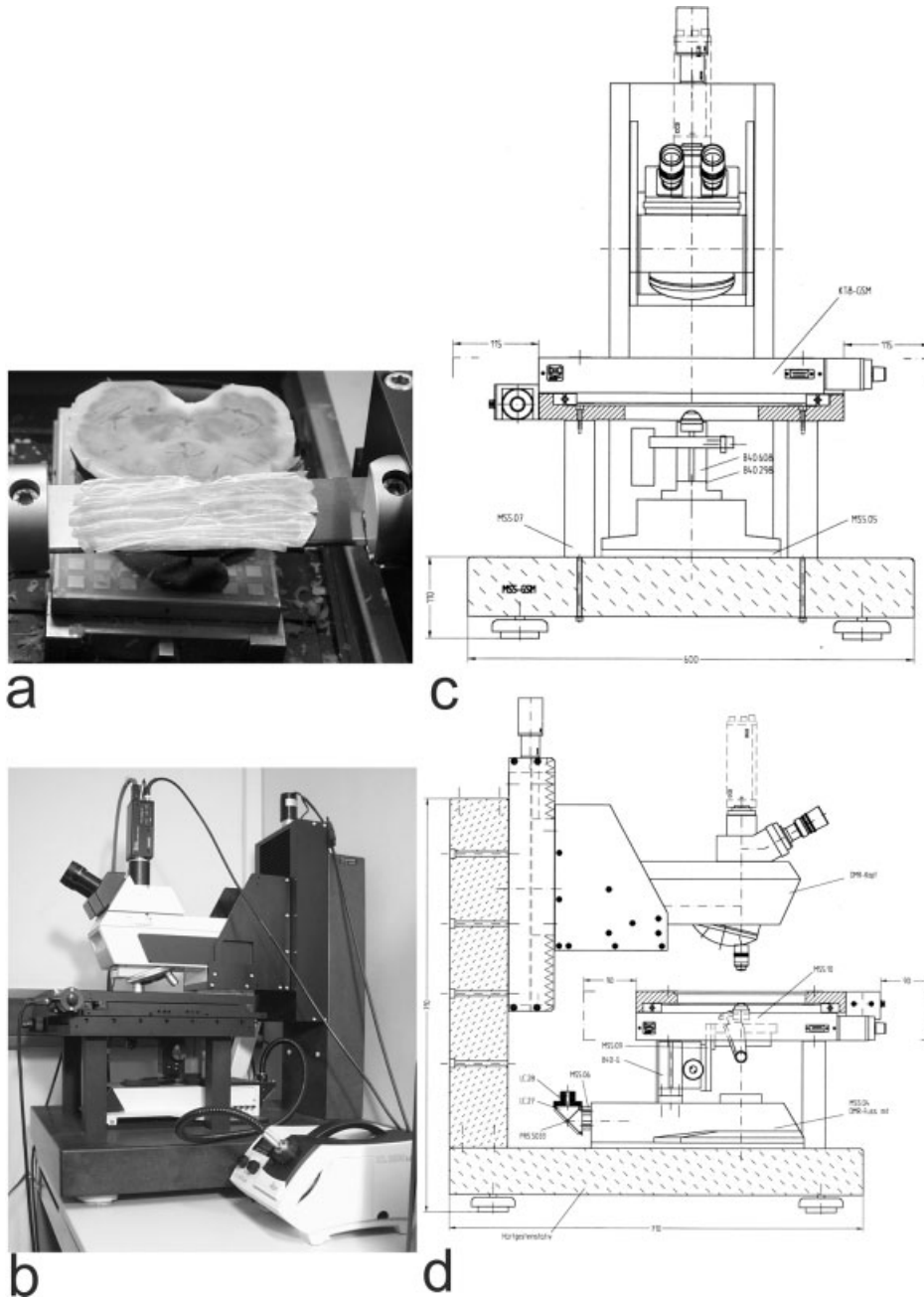


Fig. 1. **a:** A whole human brain embedded in a block of paraffin wax. A 20-µm-thick section just after cutting is still laying on the microtome knife. **b:** The very large section analyzing microscope (VLSAM) in a side view. The cold light device is standing in front

of the microscope on the right side. **c,d:** Drawings of the construction of the VLSAM. Notice that the object table is fixed on 4 columns and the head of the microscope at the z-axis motor.

rinsing them two times in distilled water, then immersing in an acidic solution (pH 1.65), and finally rinsing in distilled water. The sections were dehydrated in ascending ethyl alcohol solutions (70% to abs. ethyl alcohol) and cleared in three xylol dealcoholizing agents. For the whole deparaffining, staining, and dehydration procedure, a transport device of stainless steel was constructed in order to transport up to 50 coronal histologic sections of whole human brains (stainless steel does not interact with the galloycanin

chrome alum staining). This is important because 6,112 sections of the subject brain were produced and had to be stained. Following dehydration, we embedded the sections in Entellan[®] (Merck, 1.07961) and mounted them under a special cover glass (thickness: 0.13–0.16 mm, 145 × 145 mm², Menzel). The polymerization of Entellan[®] over such a large area (145 × 145 mm²) under the cover glass takes up to 6 months. However, we found that sections can be processed by a videomicroscope if the mounting medium is not too thick.

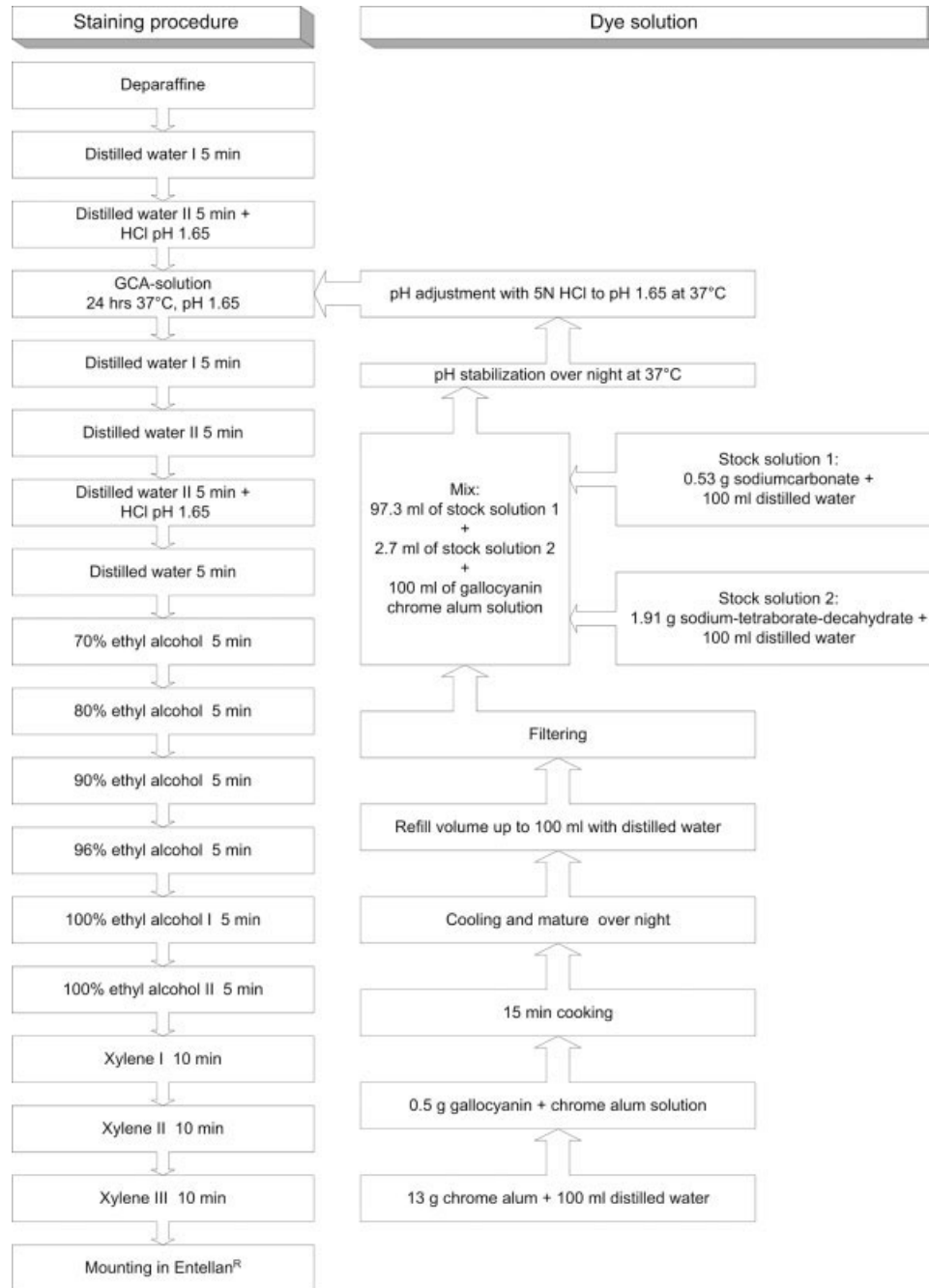


Fig. 2. The gallocyanin chrome alum staining protocol for staining histologic sections of whole human brains is shown.

Very Large Section Analyzing Microscope (VLSAM)

The VLSAM (Fig. 1b) was constructed on the basis of a DMR light microscope (Leica[®], Wetzlar). The microscope head (Fig. 1c,d) was detached from the original microscope stand and fixed to the new stand to which the z-axis stepper motor also was fixed. The microscope base was assembled on a plate of hard rock (density: 3 kg/dm³, elastic modulus: 10⁵ N/mm², linear expansion coefficient: 5–7.5 × 10⁻⁶ 1/K, hard-

ness; Mohs scale: 6–7). The optical system consisted of an infinite optic. Illumination could be adjusted according to Köhler (James and Tanke, 1991). In order to reduce thermic deformation of the microscope over very long processing periods (≥30 days), a cold light source (KL 2500 LCD, Schott) was assembled to the VLSAM (Fig. 1b) via an 8-mm light guide. On the head of the microscope, the 3-chip RGB CCD-video camera (XC-003P, Sony[®]) was attached. The engineering drawing of the VLSAM is shown in Figure 1c and d.

The xy-axes stepping motors are fixed at the microscope stage. The traverse path is 250×250 mm large, and the x-y-resolution is 250 nm. The z-axis motor has a traverse path of 50 mm and a resolution of 25 nm. Flatness and angularity are essential for an even fixation of the microscope base, however, the measurement protocol is not presented here. The three motors are controlled by a motor control processor (MCP 3/4, Zeiss-Vision[®]). These motors could be controlled manually by a joystick at the control console or automatically by software. The video camera transmitted the PAL signal to a framegrabber (Meteor PPB-RGB, Matrox[®]) in a 400-MHz PIII computer (*imageserver*). On the imageserver, the image analysis toolbox KS400 from Zeiss-Vision processed the incoming image data.

Image Processing and Control of the VLSAM

Control of the VLSAM and the data acquisition was realized over several operations on two different scales in order to assure an efficient analysis of the final resolution at the cellular level. These operations produced results from the generation of a low-resolution motor positioning map (*L-map*), a high-resolution motor positioning map (*H-map*), and the automatic focus routine. How these positioning maps are obtained and how the automatic focus routine was realized are described in detail later in this article.

Initially, the slides were fixed on a frame under the microscope and the illumination was adjusted using a $5\times$ objective (magnification at $23 \text{ cm} \times 16 \text{ cm}^2$ large window: $\times 230$, resolution $1.26 \mu\text{m}/\text{pixel}$). The sections on the slides needed to have all the same orientation. Thus, the upper convexity of the two hemispheres was oriented in the respective direction of microscope stand.

A macro (*generate-map*) was developed using the KS400 system (Zeiss-Vision[®], Jena) to define the projected upper left corner and the lower border of the FIBS (see Fig. 4c) and store the coordinates for later purposes in a database (*basedata*). After navigating around the section and defining a rectangular region around it, we shifted the upper left corner into the focus plane. Thereafter, the section was shifted systematically in a meandering fashion (Fig. 3) in an effort to find all those regions that contained tissue. This preparative step was necessary to help reduce the mass of data for analysis at the final magnification of $\times 1,850$. After each shift, a gray level image was captured and analyzed with respect to its content. If the pixel sum exceeded a certain threshold, it was probable that only the light background outside the section had been captured. Such a position of the section in the focus plane would not be written into the final motor map; those section positions would only be registered under tissue structure that had been detected at a low resolution (objective $5\times$, $1.26 \mu\text{m}/\text{pixel}$). For each section, such a tissue location list, respective motor positioning map (*Lmap*, *mpos_5*), was calculated and could be reused for further evaluations (Fig. 3).

The final resolution was $0.12 \mu\text{m}/\text{pixel}$ at a magnification of $\times 1,850$ at a $23 \times 16 \text{ cm}^2$ large window using a $40\times$ objective. An image of the background without any tissue structures or artifacts was grabbed at defined illumination conditions (the cold light device

generated a 2,800 K light temperature), median filtered (filter size: 5×5) and used for the shading correction (Schmitt and Eggers, 1999) of the images that are processed by the system (the image processing environment consisted of more than one computer).

The macro *odysseus* was the core program for detecting and quantifying cells. It was programmed with the aid of the same software environment as the macro (*generate-map*) and made use of the *L-map* (generated by the first low-resolution exploration of the section) for shifting the section meander-like over a 8×8 position subfield (*H-map*) (see Fig. 3, top right inset), respectively, on a minimal path and targeted only to those regions where tissue structures had been previously detected. The automatic detection of those focal planes that contained biologic material was done thoroughly in order to overcome the problem of defocussing within artifacts.

After a new position was reached, the z-motor scanning stage was moved 25 steps upward from the last midway optical plane of the section space so that the new optical plane was positioned above the section surface. From here, the scanning stage was moved 50 steps in the direction of the lower surface of the section, grabbing an image after each shift (Fig. 4a,b). Each step had a metric size of $1 \mu\text{m}$ and consisted in the motor coordinate system of 40 microsteps of $0.025 \mu\text{m}$. As a result, a spatial depth of $50 \mu\text{m}$ was explored around and within each section space. Foldings, crinkles, micro- and macrocracks, and physiological holes as well as artificial holes may disturb the so-called *fine focus routine*. Therefore, a *coarse focus routine* was initiated if no structures were detected within a certain fine focussed optical plane. The exploration space within and around the section space was enlarged up to $150 \mu\text{m}$, or 7.5 times larger than the mean section thickness ($20 \mu\text{m}$). If no tissue structure is found within this exploration space, the last plane of focus where tissue structures were found was used.

The coarse routine was applied within the new scanning stage position in x-y-plane until tissue structure was detected. Then the fine focus routine was re-initiated again (Fig. 4a,b). Fine stepping through the section space from the upper to the lower surface in approximately $2\text{-}\mu\text{m}$ steps was performed after calculating the differences of standard deviations of the gray level images of the optical planes (Fig. 4b). The upper and lower surface of a cortical region of a histologic section is shown in Figure 4f.

It is obvious in Figure 4f that the surfaces do have a relative smooth distribution. All images have a rectangular geometry (764×575 pixels) according to the geometry and resolution of the CCD-sensor. By using the maximal image size that corresponds to the viewing field of the optical projection, the motor actions, therefore, the evaluation time was reduced.

The resultant image analysis was the most complex algorithmic part of the whole processing. Thus, it was distributed on a five-client computer farm. These image analysis clients (*iac*) enabled the analysis and measurement of tissue components in the grabbed images.

However, before an image from the *imageserver* (i.e., the computer system that grabbed video images and controlled the VLSAM) is sent to an *iac*, it had to be

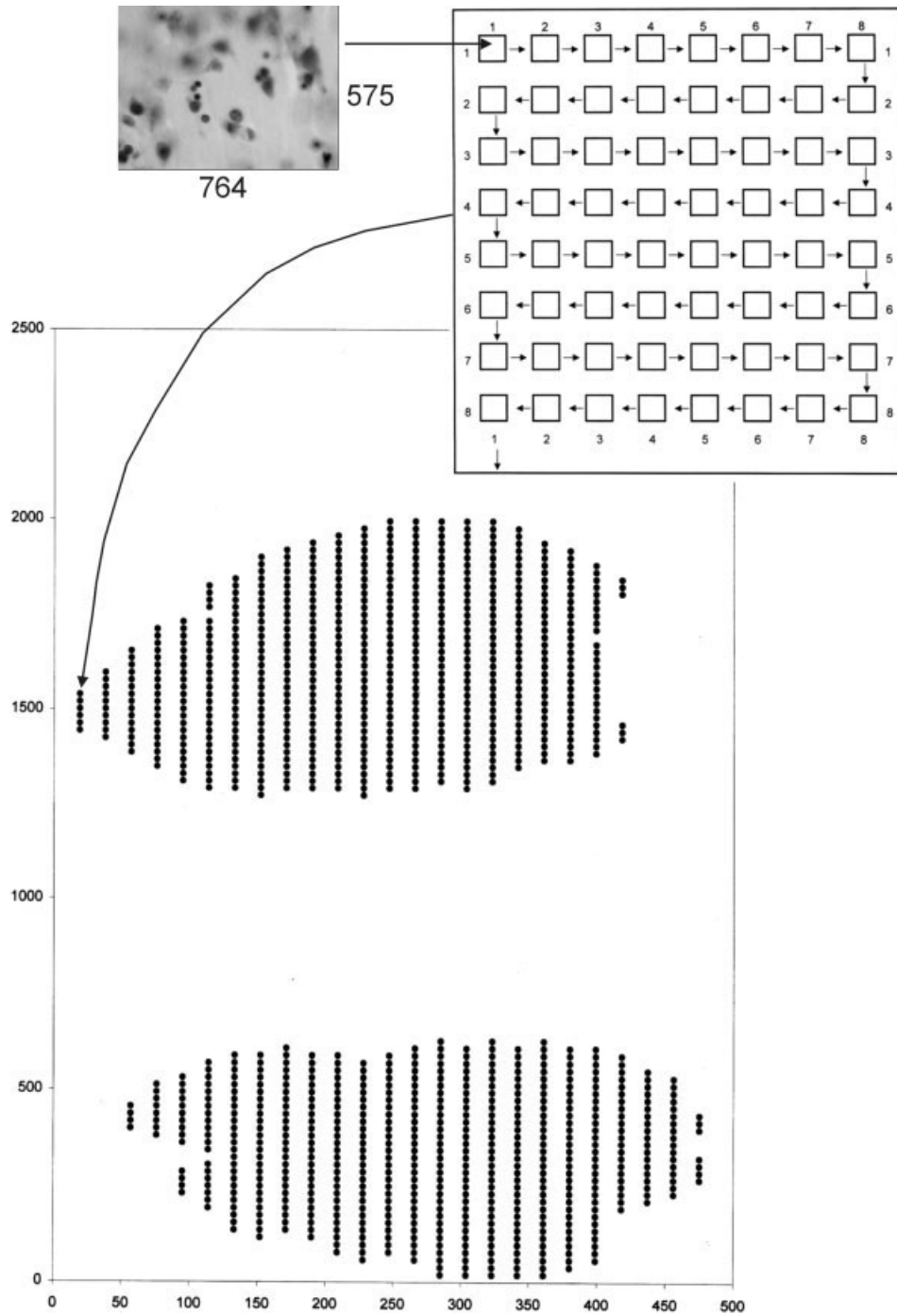


Fig. 3. **Bottom:** The (*L-map*) of a whole brain section through the both occipital lobes is shown below as a point plot. **Top right:** The fine meander-like map is presented. In this case a 8×8 position map (*H-map*) is used. Within evaluations of multiple sections, a 12×15 position map is more pertinent in order to reduce scanning stage shifts. **Top left:** Each image consists of 764×575 pixels.

tested with respect to availability. If the availability was certified by the *iac*, then the imageserver could transmit the actual image. But if an *iac* should fall out, the next available one was sought. This methodology helped to assure that the image-processing environment is fault tolerant with respect to unavailability of *iacs* and that it is upscalable.

Upscaling the hardware (e.g., adding further *iacs*) was important because the upscaling increase the processing velocity. The images (tif-format) were distributed in a circular way on five *iacs*, starting with the first one and progressing until the fifth had been reached, then starting again with the first. If a new image was received, it was loaded into a RAM-frame

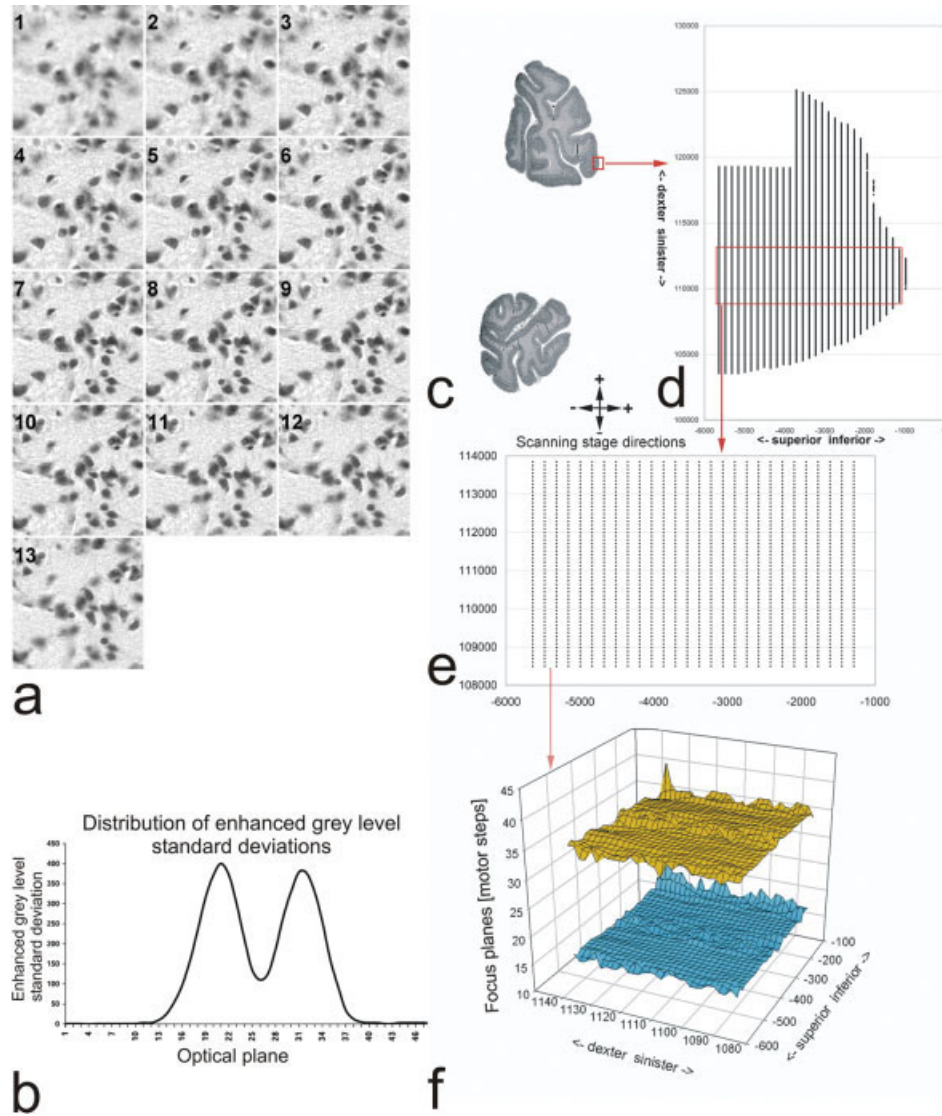


Fig. 4. Presentation of (a) a stack of 13 images of subsequent optical projection planes and (b) the distribution of transformed intensity standard deviations. The first peak is always a little bit higher and denotes the position of the upper surface whereas the second local peak is lower and indicates the lower surface of the section. The upper and the lower surface (shown in f) of a histologic section (c) that is located within the both occipital lobes. **d**: Motor position map.

The red frame indicates the rectangular region (e) over which the upper and lower surface was plotted (f). The top (yellow) and the bottom (blue) surface of this area of the histologic section show a relatively smooth course, meaning that the autofocus routine is not effected by artifacts and that the top and bottom surface of the section have a suitable quality for analysis. [Color figure can be viewed in the online issue, which is available at www.interscience.wiley.com.]

respectively image memory. Each image had a signature such as “5_800_1.tif,” which means that the image stemmed from row 5, column 800, and z position 1. Therefore, absolute coordinates of a single pixel or the gravity center of a cell can be determined explicitly.

The program was able to load image stacks of a KS400-format “x_y.zd” and work in a 3D-mode or load images of a singular z-plane “x_y_z.tif.” If the macro was started after the accumulation of images in the import directory, it took down the stack of images, image by image, independent of new images being written into the import directory and thus processed automatically after finishing the stack. In other words, the macro of the *iac* could be modified while the *image-*

server was running. For example, new segmentation algorithms could be implemented and tested in real time. We did demand a special diligence to identify and correct and/or adjust to data access conflicts. Such conflicts can emerge if an image is listed in the file allocation table but image data are still being written into the file while an *iac* macro tries to load this image. Fortunately, the automatic process of building image stacks and image loading can be overridden and then finished manually.

Image Analysis

The aim of the different procedures of image analysis applied here was the robust detection of cells and their

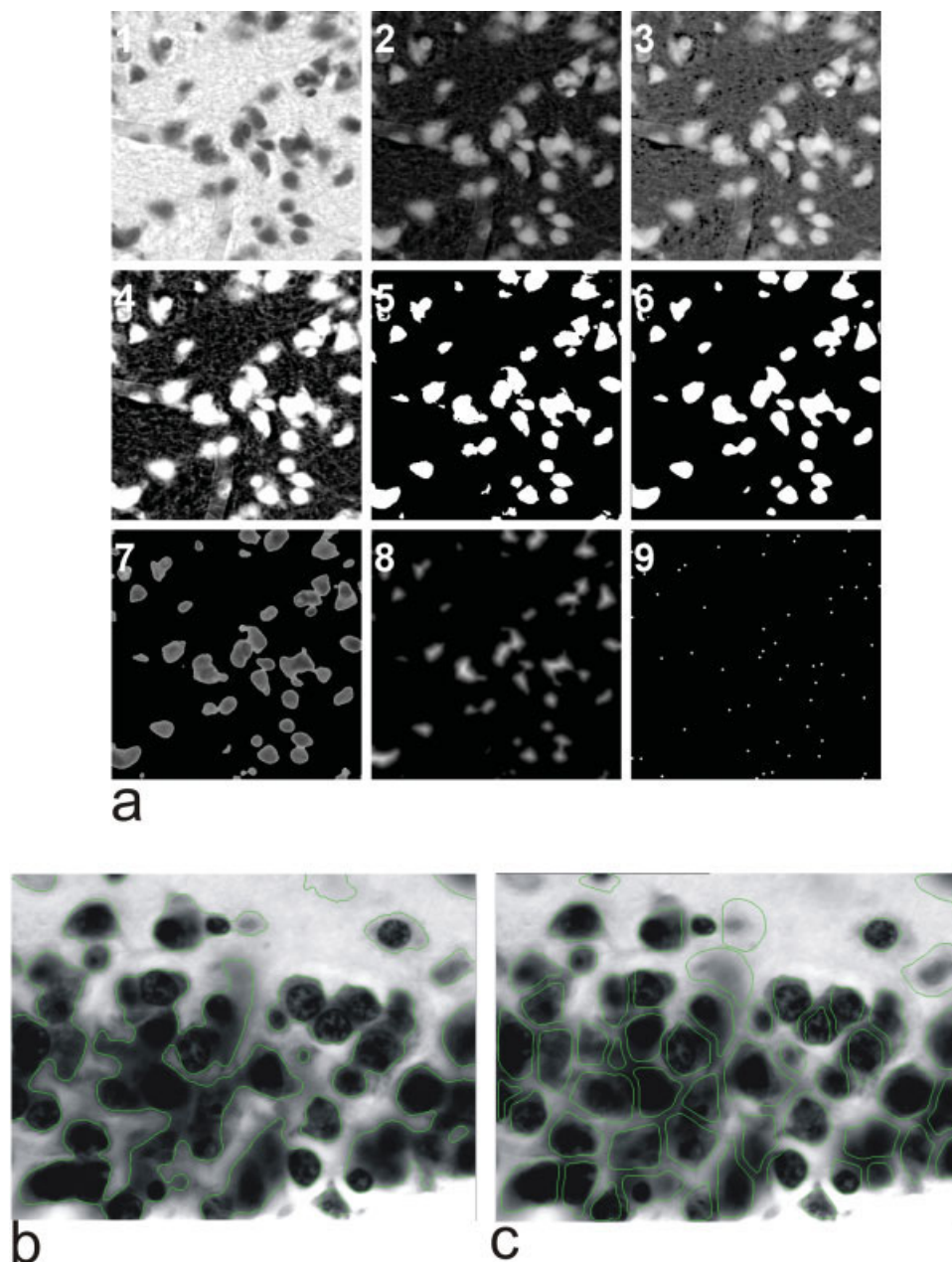


Fig. 5. **a:** Example of the segmentation and deagglomeration process of clustered cells. The image dimension used here is not used for the evaluation of the large sections. **1:** original image; **2:** inverted image; **3:** contrast enhanced image; **4:** adaptive segmentation (see text); **5:** binarization of the segmented image; **6:** median smoothed binary image; **7:** the binary image is used as a mask for the original image; **8:** distance transformation of the binary image; **9:** local maxima of the distance transformed and smoothed image. The resulting

seed points can be used as initial markers for the watershed algorithm. Example of a histogram based segmentation (b) without deagglomeration and (c) with a watershed-based deagglomeration of cells. In b 16 and in c 56 structures of interest were found. The relation of this is approximately 3.5, which means that the fast algorithm underestimates, in this example, by a factor of 3.5. [Color figure can be viewed in the online issue, which is available at www.interscience.wiley.com.]

quantitative characterization (e.g., area, perimeter, shape factor, mean grey values, variance of grey values). To detect cells in a highly complex image context, we employed different operations and steps of processing images.

The images were loaded by a KS400 macro from a specified import directory on the hard drive of a designated *iac*. The image analysis chain started with a

shading correction of the image. Yet because relatively small structures (e.g., glial cells and neurons) should be segmented on a variable background, an adaptive gray value segmentation was used. Such an approach has proved useful because most of the cell-rich foreground regions, even those that are a little bit defocused, can be segmented sufficiently (Fig. 5a).

In the resulting binary image, all areas of adjacent pixels with a number of less than 100 pixels are eliminated. The edges of the binary objects were smoothed by a median filter (7×7) followed by filling up holes in the objects by pixels with intensities of 255 (Fig. 5a).

If several binary objects were agglomerated (Figs. 5a.7, 5b), then it was necessary to deagglomerate them. This was done by applying mathematical morphology (Fig. 5a.8, a.9, b). The binary agglomerated object was distance transformed (Fig. 5a.8). The distance transformed image was low-pass filtered by a median filter of 7×7 . The local pixel intensity maxima were detected and used as seed points (Fig. 5a.9) for subsequent watershed transformation (Dougherty, 1993). The original image was low-pass filtered (11×11), and the watershed transformation with the seed point image was performed.

Another more complex example is given in Figure 5b. If too low filter sizes were applied, an oversegmentation of cells would appear. However, deagglomeration is a time-consuming computing procedure. Therefore, we decided to perform analysis without (fast mode, Fig. 5b) or with the deagglomeration step (slow mode, Fig. 5c).

After segmenting and deagglomerating, the cells or objects were ready to be measured. But we selected for measurement only those cell-profiles that did not hit the forbidden line as introduced by Gundersen (1977) (Fig. 6a), otherwise a strong overestimation would have been introduced by the system. The forbidden line was defined in the 764×575 pixels large images as a centered frame of $(764-128)$ pixels \times $(575-128)$ pixels size (Fig. 6a). The distance of the counting frame from the image border to all sides of the image was 128 pixels large. Using this frame size, large pyramidal cells can still be acquired. Additionally, because different projection planes were imaged, the cell profiles within each plane were detected. According to the size and spherical, elliptical, or pyramidal form of most cells in the CNS, it was possible to automatically determine cell profiles by evaluating the area distribution of each cell separately over all images of the scanned image planes (Fig. 6b). We selected only those cells that were located completely within the section space or that touched the upper surface of the section (e.g., the first image of the image stack) with any part of their projections. The x-y-motors move the scanning stage of the microscope exactly to the congruent border of the adjacent counting frame, not to the next congruent image border.

After selecting cell profiles according to the rule of the forbidden line their area, perimeter, coordinates of the gravity center, the shape factor, the mean gray level, and variance of gray levels were determined. Finally, the data were added to a local database on the *iac*. They were read out of the databases of the five *iacs* and transferred to the visualization package persistence of vision *povray* (<http://www.povray.org>) for presentation.

Image Registration

As is apparent from Figure 1a, the sectioning processes lead to non-linear deformations of the tissue sections. Additional distortions are introduced by the dehydration and the embedding process. The paraffin wax embedded brain is regarded as a homogenous elas-

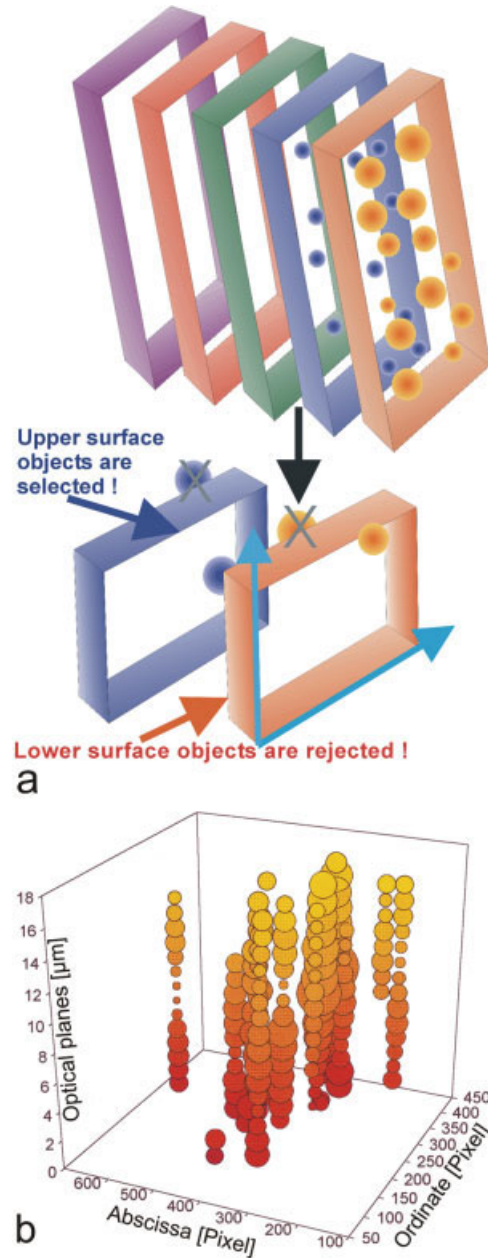


Fig. 6. The concept of forbidden line was implemented in the quantification procedure and is illustrated here (a, top). It is important to extend the original for two dimensions defined technique to three dimensions. Only those cells were counted that do not touch the forbidden lines. The forbidden lines are shown in green in an original image. Cells that touch the blue lines are retained for further evaluations. b: A graphical representation of the three-dimensional distribution of cell projections within succeeding optical projection planes (triplanar 2D). Because of the spherical, ellipsoid, and pyramidal forms, it is unambiguous if cells are cut by the top or bottom surface of the section. This information is necessary to apply the concept of forbidden lines in three dimensions.

tic material. Thus, we take advantage of an elastic registration in order to mimic the type of the deformations used to correct the high-resolution transparent flat-bed-scans of the sections; e.g., Modersitzki and Schmitt (2001); Modersitzki et al. (1999); Modersitzki (2004); Schmitt et al. (1999).

Here, we model the deformations using a standard approach of linear elasticity theory; e.g., Landau and Lifshitz (1959); Broit (1981); Gurtin (1981); Bajcsy and Kovacic (1989); Miller et al. (1993); Christensen et al. (1994); Bro-Nielsen and Gramkow (1996); Schormann et al. (1996); Ciarlet (2000); Modersitzki (2004). To this end, we denote the scan of a section k as a *reference* and the scan of the consecutive section $k + 1$ as a *template*. We then compute an elastic transformation, such that the so-called L_2 -distance between the reference and the transformed template becomes minimal. The transformed scan then serves as a reference for the correction of the scan $k + 2$. This procedure is started with the scan of maximal area (number of non-background pixels).

Using the variational method, a minimizer can be characterized by the so-called Euler-Lagrange equations, which for this particular situation are also known as the Navier-Lamé equations; e.g., Landau and Lifshitz (1959); Broit (1981); Gurtin (1981); Bajcsy and Kovacic (1989); Schormann et al. (1996); Modersitzki (2004).

Finally, resulting system of non-linear partial differential equations has to be solved numerically. A fixed-point type iteration bypasses the nonlinearity and a finite difference approximation of the remaining linear partial differential equations results in a huge but highly-structured finite dimensional system of linear equations. The intrinsic discretion of an $m \times n$ pixel image results in a system of linear equations for $2mn$ unknowns. Thus computational time and memory requirements play an important role. Therefore, Fischer and Modersitzki (1999, 2001) have developed a fast solution scheme based on the Fast Fourier Transform (FFT). This algorithm has also been implemented to a parallel high-performance computing cluster (Böhme et al., 2002). A detailed description of this parallel implementation for a 48 dual pentium cluster was published by Modersitzki et al. (1999).

RESULTS

At first, the fine and coarse motor positioning maps were controlled over a whole large histologic section. The result of the more important (*H-map*) based positioning is shown in Figure 7. It was generated in such a way that the computed so-called motor coordinates were written into the maps shown in Figure 7a. The red and green squares consist of 8×8 pixels.

Such a whole square presents a coordinate in the (*L-map*), whereas a single pixel of the square illustrates the position of an image at the final resolution. Each pixel is marked due to the appropriate motor-position and, therefore, indicates the absolute position on one image of the size of 764×575 pixels. We chose two different colors in order to differentiate between adjacent 8×8 -pixel squares. If the positions are exactly congruent to each coarse and each fine position, no distortions of the green and red rectangles should appear. This is the case for Figure 7aa. However, if small non-congruencies appear, the congruency map displays pixel-wise shifts (Fig. 7aa and ab). Using the correct shifting procedure, a high-resolution map or *image mosaic* can be constructed in which no overlaps or systematic shifting errors can be seen (Fig. 7b). This subfigure (Fig. 7b) consists of 3×3 coarse motor position field indicated by the three red, three blue, and three green fields. Each of these coarse fields contains 12×15 fine motor positions

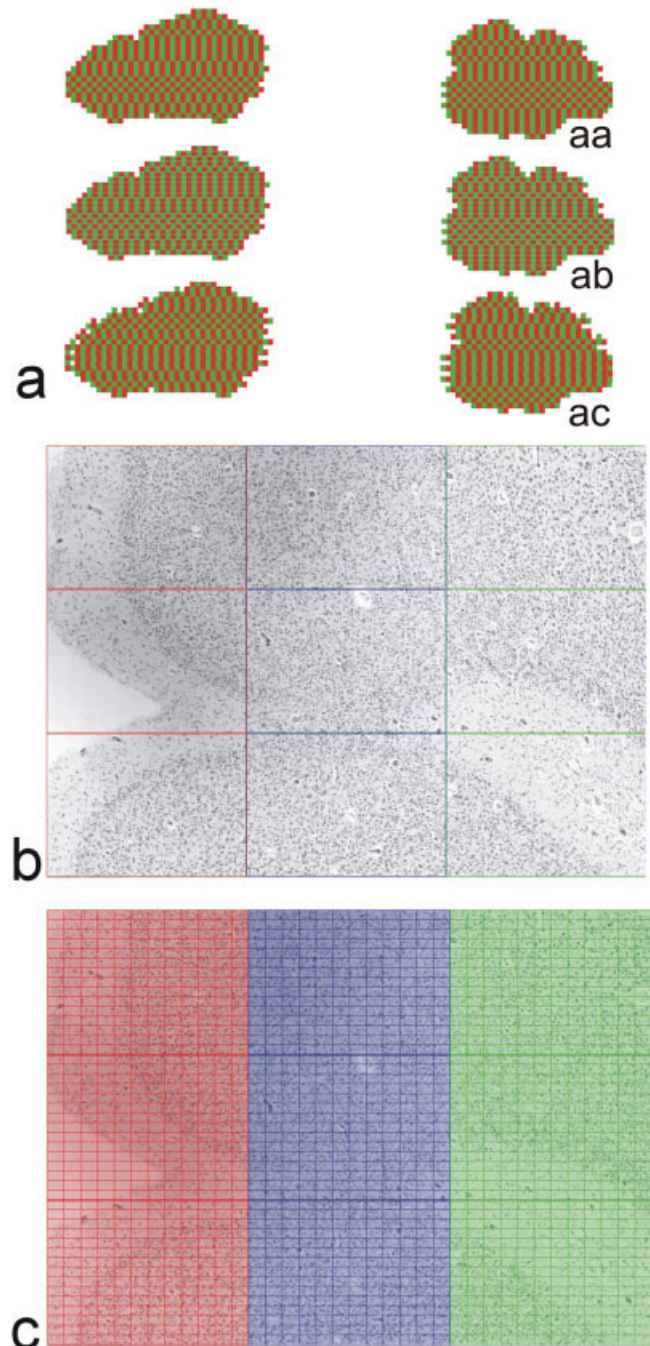


Fig. 7. **a:** In order to verify the exact congruency of the shifting schemes *coarse* and *fine*, the motor positions are mapped as red and green pixels. **aa:** An exact working technique (aa) whereas both lower examples (ab, ac) display distortions. **b:** An image mosaic generated by the same shifting scheme as applied in a) is generated here. Each of the three rectangular red, blue, and green regions contain **(c)** 12×15 images of the size 575×764 pixels. [Color figure can be viewed in the online issue, which is available at www.interscience.wiley.com.]

(Fig. 7c) at which an image of the size of 764×575 pixels were assembled. Therefore, the whole mosaic presented here has a size of $3 \times 3 \times 12 \times 15 \times 764 \times 575$ pixels (7.11666×10^8 pixels). The sections 115 to 119 from the series 1 to 6,112 were analyzed as described

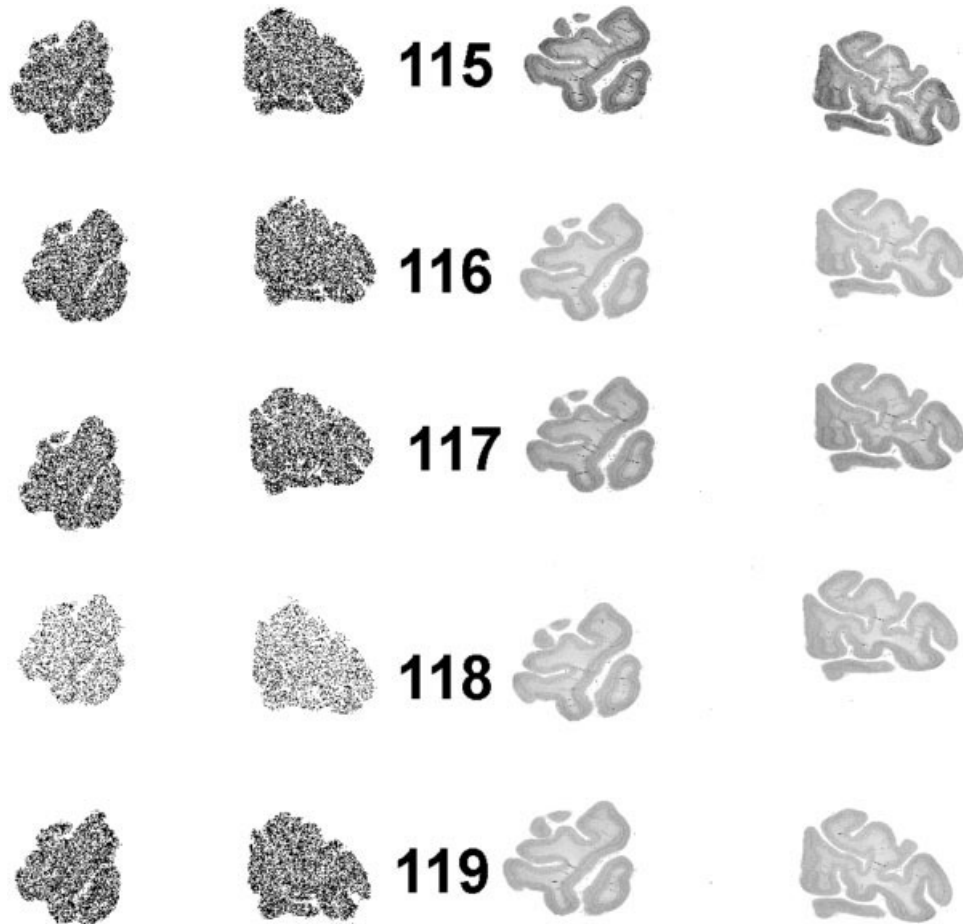


Fig. 8. The five sections 115 to 119 have been completely scanned by the VLSAM applying the fast algorithm. **Left:** The distributions of every 40th gravity center of the cells and cell-clusters are plotted. **Right:** The flat bed scanned histologic sections are presented. Please notice that section 118 is slightly thinner and, therefore, the cell density declines in the object data plot.

above (Fig. 8). In each section, approximately 8×10^5 cells (neurons, glial cells, and other cells) were detected. Every 40th individual cell was plotted (Fig. 8) to get an overview of the detected locations of cells. Otherwise, plotting each gravitation center of the detected cells would lead to an image containing a homogenous black section because the cell density is too large for reproduction. The selection of every 40th cell was done in the way they appear in the data file. A further visualization was calculated with *povray*. In *povray*, the cell diameter was used to illustrate cells as spheres of appropriate size. Spheres were located at the gravity centers of the measured cells. Depending upon their mean gray intensities, they were color coded (Fig. 9).

Due to sectioning, mounting, staining, embedding, and fixation of the microscope slides on the scanning table of the microscope, the resulting object data can not be displayed directly in three dimensions because the mentioned procedures introduce different kinds of linear and nonlinear distortions on each section. Thus, we applied a registration technique that matches the distorted data. As an example, we present here registered object data in a region of interest located within the transition region of areas 17 to 18 (Fig. 10). The

lamination is visible in the object data plots (Fig. 11). Lamina 1 as a pale layer is characterized by its low cellular density, whereas other layers display a clearly visible larger packing density of somata. The white matter border is conspicuous, too.

The left hemisphere of section 115 has a cortical area of $1,452.68 \text{ mm}^2$ and a volume of 29.05 mm^3 . The white matter area is 748.37 mm^2 and the volume is 14.97 mm^3 large. The whole section area has a size of 2201.05 mm^2 and a volume of 44.02 mm^3 .

DISCUSSION

A new light microscope, the very large section analyzing microscope (VLSAM), and a parallelized image analysis system was developed to quantify all cells (neurons, glia cells, and other cells) of single human brains. The VLSAM proved to be a highly effective, accurate, and revelatory system.

Worldwide, a comparable light microscope is not available for continuously scanning through histologic sections of a whole human brain at a high spatial resolution. The reason for this is the fact that coronal sections at the position of the temporal lobe (where they

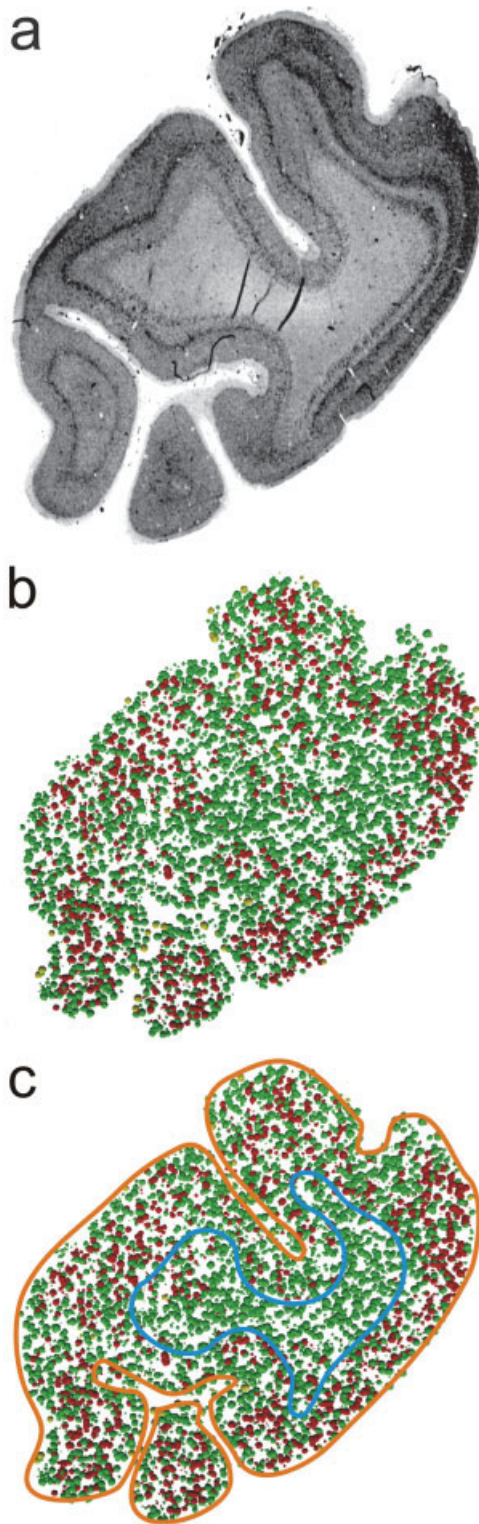


Fig. 9. After analyzing the databases of the evaluated cells, more parameters can be visualized. The size of the cells, their gravity center and the color-coded (intensive stained nuclei of glia cells are green and less stained perikaryons of neurons are red) mean gray values of the cell profiles are shown here. The gray matter and the white matter as well as their borders are clearly visible. **a:** The section in which cells displayed in **b** and **c** were detected. Every 40th cell was selected here to get an overview of the cell distribution. **c:** The cerebral cortex is located between the outer red and the inner blue line.

have their largest extension) through the whole human brain have an area in the embedded situation of up to $130 \times 130 \text{ mm}^2$. Such a large area cannot be shifted by an x-y-scanning stage because the distance between the backward edge of the y-axis part of the scanning stage would collide with the tripod of commercially available bright field light microscopes. In a first approach, we have shown that the positioning of the section is reproducible and regular. However, further measurements and comparisons with an external standard of known geometry will be necessary for determining the exactness of the stepping procedure.

Comparable concepts have been reported by McCormick (2002), Koh (2000) and Sutoo et al. (1998). Yet McCormick (2002) and Koh (2000) developed a system that can only be applied to small brains such as those of mice and rats. A microphotometry system in epifluorescence mode that is able to shift a section over an area of $150 \times 150 \text{ mm}^2$ has been developed by Sutoo et al. (1998), but this device does not need a condenser, thereby making it difficult to adapt to a microscope with a large scanning stage.

In our study, registered images were not warped to a standard coordinate system to better facilitate comparative studies for investigating interindividual variabilities (Amunts et al., 2000) on different scales. Warping-registered high-resolution images of histologic sections to the Talairach coordinate system (Talairach and Tournoux, 1993) will cause problems (e.g., loss of information caused by interpolation) due to the relative coarse resolution of this reference system. The Talairach stereotaxic coordinate system was originally developed for neuroradiologic diagnosis and neurosurgery therapies based on serial sectioned postmortem human brains and MRI-images. A total of 58 serial coronal sections per brain was used, providing a sample base that is suitable for generating a reference system for stereotaxis. The reference system is based on the CA-CP line (commissura anterior–commissura posterior) that defines the horizontal plane and two vertical lines (VCA, VCP) that intersect the CA-CP at the CA and CP. Because the CA and the CP are lying relatively close together (the length of a human brain is about 13 cm, the distance between CA and CP is about 2.5 cm), this reference system may experience larger deviations around the rostral parts of the frontal lobe and the occipital parts of the occipital lobes. Hence, warping a registered three-dimensional high-resolution dataset (magnification 1,850 \times) to the Talairach reference system will cause inaccuracies that should be avoided if the intent is to generate a precise model of gravitation centers of neurons. Furthermore, the variability and differences of the brain sizes and CA-CP values between the sexes are not sufficiently taken into account. Therefore, the human brain atlas (*The Human Brain Atlas*, Karolinska Institute) seems more appropriate for comparative studies of interindividual cytoarchitectonics (Geyer et al., 2001; Roland et al., 1994; Roland and Zilles, 1994; Schormann and Zilles, 1997, 1998).

Yet it should be noted that the *Human Brain Atlas* is the mean of a population of MRI-scanned brains. The contrast of the *Human Brain Atlas* must be reduced (due to averaging) in comparison to original data of the individual brains. For studies of structural and functional parcellation of areas of the cerebral cortex, this seems not to be crucial (Geyer et al., 2001). The data

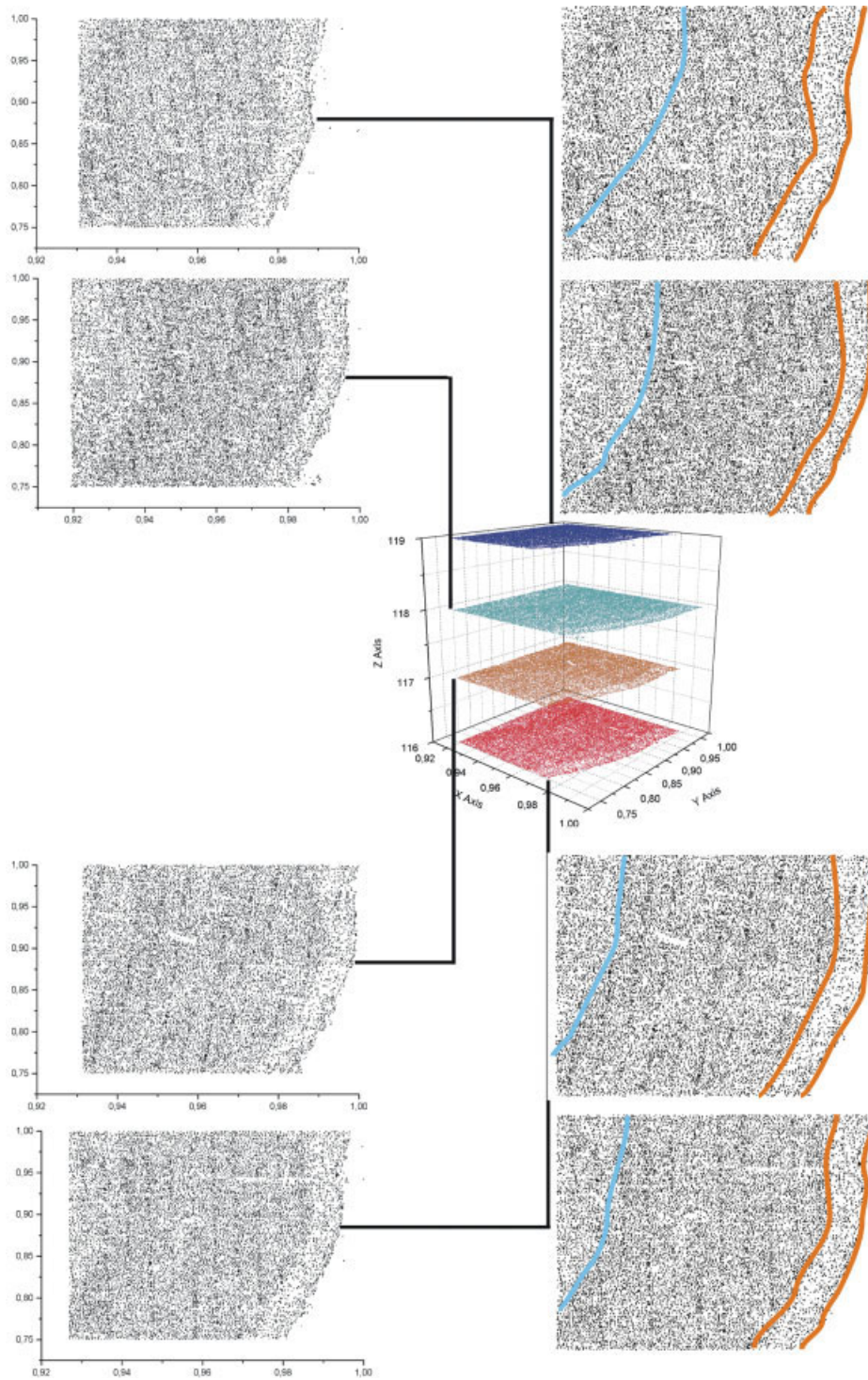


Fig. 10. The object data has been registered by a nonlinear matching algorithm based on elasticity theory. This is necessary because the sections possess different kinds of linear and nonlinear distortions. Otherwise, the object data of adjacent sections would not match together in a three-dimensional object data model. A ROI is presented here as an example of how neurons are distributed in a virtual three-dimensional space. Note that lamina 1 (in between the red lines) and the white matter border (blue line) that have been marked on the right side are visible in the registered object data plots. [Color figure can be viewed in the online issue, which is available at www.interscience.wiley.com.]

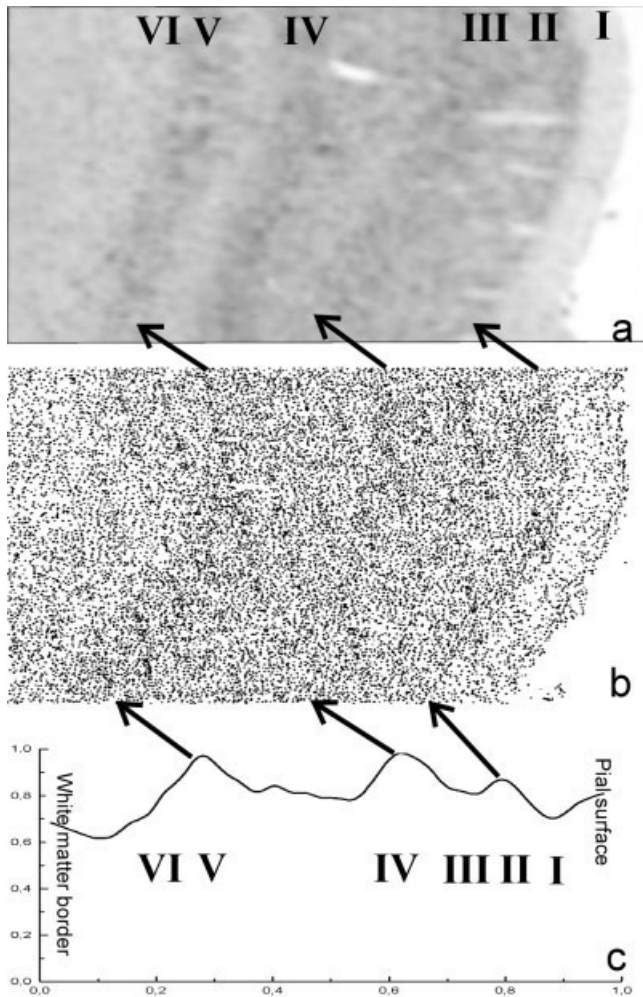


Fig. 11. **a:** A ROI of the registered section no. 118. The same region is displayed in **b** as a dot plot of the gravitation centers of the detected cells. **c:** The mean profile of this cerebral ROI is presented. The main layers I to VI can still be detected in the profile plot (Schmitt and Böhme, 2002; Schleicher et al., 2000) of gravity center distribution datasets. Layers with high cell densities are connected by arrows in between the panels.

derived from the neuronal scale represent microscopic details and individual cell features rather than those coarse features of cell profiles that are sufficient for recent cytoarchitectonic studies (Amunts et al., 1999ab, 2000; Geyer et al., 2001; Schmitt and Böhme, 2002; Schmitt et al., 2003). Therefore, we have to find a suitable transformation of the lower resolved and averaged *Human Brain Atlas* to the high-resolution object database and vice versa.

Due to sectioning and histologic procedures, single sections may get lost. Naturally, this is the case in the series we made. Currently, there exists no alternative for handling histologic sections without loss of sections. As a consequence, the technique presented herein should be considered as a first major step toward free-of-loss and complete brain modeling at the neuronal level.

The deagglomeration of cell clusters is the most time-consuming part of the image analysis. Therefore,

the sections can be evaluated in two modes: a fast mode where deagglomeration is inactivated and a slow mode where cell clusters are deagglomerated by a filtering, watershed, and binary restoration scheme. The cellular objects in the resulting segmented and deagglomerated binary images are automatically morphometrized and the data are written into distributed databases, which can be combined after or within the evaluation.

The cell counts of the VLSAM have been compared with those that were found by Haug (1984) who determined the mean density of cortical neurons and glial cells to be $6.92 \times 10^4/\text{mm}^3$. Blinkov and Glezer (1968) reported a mean density of glia cells within the white matter of $1.283 \times 10^5 \text{ mm}^3$. As mentioned earlier (see Results), we found in the whole section 115 (area: $2,201.05 \text{ mm}^2$, volume: 44.02 mm^3) 8×10^5 cells (neurons, glial cells, and other cells). Comparing the quantification of Haug, Blinkov, and Glezer with these data, we found a factor of 4.91 times underestimation. This is because we used the fast evaluation mode, which does not deagglomerate data. In Figure 5b, the fast algorithm detects 3.44 times less cells. However, we applied the deagglomeration algorithm to a region with a very complex cell distribution and with many overlaps of optical projections, e.g., the fascia dentata of the hippocampus.

Because the somata of neurons are still large with respect to glial cells and glial cells do emerge to a lesser extent in this part of the hippocampus, the algorithm does not reach a 4.91 mismatch. Due to different counting procedures and stereologic calculations, an overestimation of cells may contribute to the mismatch, as well.

The area of cells has been determined, also. Due to positioning of the brain within embedding in paraffin wax, positioning of the paraffin block on the microtome, and a high degree of anisotropy of cells, they were not cut perpendicular to their longitudinal axes. Therefore, the size estimation is biased if only one optical plane is considered.

Yet, as shown, we have the ability to perform serial optical sectioning within a section. Therefore, we can estimate unbiased volumes of individual cells. The three-dimensional section space analysis uses 10 to 15 times more computing resources. Thus, we can dispense with the unbiased variant in order to present an overview of this approach.

So far, the quantities of whole brain sections are only available for the prototypical fast algorithm. However, currently MATLAB scripts (Mathworks) and C programs are developed for accelerating image processing and augmenting accuracy of cell recognition. As a result, the plots of gravitation centers must be viewed as an approximation of the real physical situation. The presentations shown here for the first time are sights of individual neuron mappings of whole brain sections at a resolution that is adequate for imaging the structural and functional entities of the central nervous system.

For the present, only one cell population consisting of neurons, glial cells, and other cells (e.g., endothelial cells, blood cells) were registered. Furthermore, the cell population was not related to the gray or white matter in order to calculate specific compartmental and cell type quantities. Such an analysis would require a

delineation of the cerebral cortex and the white matter as well as a sophisticated pattern recognition operation for classification of the different cell types. Meanwhile, such a classification operator has been developed (Rist, 1999). However, the artificial neuronal network (network topology: 2 hidden layers, backpropagation learning rule) must be optimized with respect to recognition accuracy and speed.

The object data were visualized as a point process where only gravitation centers of the cells were plotted or as a multidimensional particle system where additional morphological features were visualized. Comparable visualizations have been published by Skoglund et al. (1993, 1996) and Schmolke (1996). Additionally, Schmolke has determined dendrites and axons beneath cellular profiles in the cerebral cortex and visualized these data in an integrative view.

To date, dendroarchitectonics and axoarchitectonics in histologic sections of the whole human brain at the cellular scale have not been quantified. Recently, a technique was presented by Pakura et al. (2002) to quantify these modalities to obtain information of large-scale wirings of the human brain.

Beside the cellular or cytoarchitectonic modality, all other modalities can be mapped in whole brain sections, which can be visualized adequately in histologic sections and are detectable by bright field microscopy. Even those visualizations that need dark field microscopy or epifluorescence microscopy (Sutoo et al., 1998) may be quantified in whole brain sections because the VLSAM can be equipped with additional optical devices. Still unsolved are the problems concerning the computation time and reliability of cell recognition. We are trying, therefore, to expedite the image processing. An encouraging approach is the grabbing of images "on the fly" within section space scanning and restoring them by a subsequent deconvolution function to avoid distortion. Such a digitalization improves the scanning velocity and delivers three-dimensional data of the section space that can promote the segmentation, deagglomeration, and recognition of cells.

Morphometrized neurons that are characterized by a couple of basic morphologic features can be artificially completed by dendritic, axonic, and synaptic simulation. Maybe such an approach can be extended in the future to simulate metabolic networks of individual neurons (Ravasz et al., 2002; Strogatz, 2001). Similar simulations have been published (Ascoli, 1999; Ascoli et al., 2001; Burke et al., 1992; Bush and Sejnowski, 1993; Hamilton, 1993; Senft and Ascoli, 1999). These models can be used for a deeper understanding of the normal and pathologic processing of neuronal information on large scales close to functionally relevant biological microspace. Moreover, such an extensive point process or particle system can be explored with regard to the geometry of cytoarchitectonic fields. The cytoarchitectonically defined areas can be easily quantified, as well as the lamination pattern, naturally by unbiased full automatic counts and the resulting absolute numbers. The intrinsic geometry of connectivity (Cherniak, 1992, 1994, 1995; Felleman and van Essen, 1991; Murre and Sturdy, 1995; Young, 1992, 1996) can be investigated by appropriate spatial clustering and geometric combinatorial techniques.

ACKNOWLEDGMENTS

We thank U. Almert, P. Lau, and E. Mecke of the Institute of Anatomy (University of Lübeck) for their excellent histological preparations, digitizing, and data administration, and W. Kühnel (Institute of Anatomy, Medical University Lübeck) for his extensive support. We appreciate the help of U. Blohm and K. Zilles (Vogt Institute, Heinrich-Heine University, Düsseldorf) who gave us valuable devices for embedding and handling of sections of whole human brains. We express our gratitude to A. Wree (Institute of Anatomy, University Rostock) for his important suggestions and critical discussion of this study. M. Limberg was of great help in editing and correcting the manuscript.

REFERENCES

- Amunts K, Schleicher A, Bürgel U, Mohlberg H, Uylings H, Zilles K. 1999a. Broca's region revisited: cytoarchitecture and intersubject variability. *J Comp Neurol* 412:319–341.
- Amunts K, Schormann T, Mohlberg H, Malikovic A, Zilles K. 1999b. Location, asymmetry and variability of human areas 17 and 18. *NeuroImage* 9:861.
- Amunts K, Malikovic A, Mohlberg H, Schormann T, Zilles K. 2000. Brodmann's areas 17 and 18 brought into stereotaxic space: where and how variable? *Neuroimage* 11:66–84.
- Ascoli GA. 1999. Progress and perspectives in computational neuroanatomy. *Anat Rec* 257:195–207.
- Ascoli GA, Krichmar JL, Scorcioni R, Nasuto SJ, Senft SL. 2001. Computer generation and quantitative morphometric analysis of virtual neurons. *Anat Embryol* 204:283–301.
- Bajcsy R, Kovacic S. 1989. Multiresolution elastic matching. *Comput Vision Graph Im Proc* 46:1–21.
- Ballard DH. 1986. Cortical connections and parallel processing: Structure and function. *Behav Brain Sci* 9:67–120.
- Barlow HB. 1986. Why have multiple cortical areas? *Vision Res* 26:81–90.
- Blinkov SM, Glezer II. 1968. *Das Zentralnervensystem in Zahlen und Tabellen*. Jena: Gustav Fischer.
- Böhme M, Hagenau R, Modersitzki J, Siebert B. 2002. Non-linear image registration on PC-clusters using parallel FFT techniques. Technical Report SIIM-TR-A-02-08, Institute of Mathematics, Medical University of Lübeck, Lübeck, Germany.
- Bro-Nielsen B, Gramkow C. 1996. Fast fluid registration of medical images. *Lect Notes Comput Sci* 1131:266–276.
- Brodman K. 1909. *Vergleichende Lokalisationslehre der Grosshirnrinde in ihren Prinzipien dargestellt auf Grund des Zellenbaues*. Leipzig: Barth.
- Broit C. 1981. *Optimal registration of deformed images*. Ph.D. thesis, Computer and Information Science Department, University of Pennsylvania, Philadelphia, PA.
- Burke RE, Marks WB, Ulfhake B. 1992. A parsimonious description of motoneuron dendritic morphology using computer simulation. *J Neurosci* 12:2403–2416.
- Bush PC, Sejnowski TJ. 1993. Reduced compartmental models of neocortical pyramidal cells. *J Neurosci Methods* 46:159–166.
- Cherniak C. 1992. Local optimization of neuron arbors. *Biol Cybern* 66:503–510.
- Cherniak C. 1994. Component placement optimization in the brain. *J Neurosci* 14:2418–2427.
- Cherniak C. 1995. Neuronal component placement. *TINS* 18: 522–527.
- Christensen G, Rabbitt R, Miller M. 1994. 3-D brain mapping using deformable neuroanatomy. *Phys Med Biol* 39:609–618.
- Ciarlet PG. 2000. *Mathematical elasticity*. Elsevier Science.
- Dougherty ER. 1993. *Mathematical morphology in image processing*. New York: Marcel Dekker.
- Duijnhouwer J, Remme MWH, van Ooyen JvP. 2001. Influence of dendritic topology on firing patterns in model neurons. *Neurocomputing* 38.
- Felleman DJ, van Essen DC. 1991. Distributed hierarchical processing in the primate cerebral cortex. *Cerebr Cortex* 1:1–47.
- Fischer A, Modersitzki J. 1999. Fast inversion of matrices arising in image processing. *Num Algo* 22:1–11.
- Fischer A, Modersitzki J. 2001. A super fast registration algorithm. *BVM* 22:168–173.

- Geyer S, Schleicher A, Schormann T, Mohlberg H, Bodegård A, Roland P, Zilles K. 2001. Integration of microstructural and functional aspects of human somatosensory areas 3a, 3b, and 1 on the basis of a computerized brain atlas. *Anat Embryol* 204:351–366.
- Gundersen H. 1977. Notes on the estimation of the numerical density of arbitrary profiles: the edge effect. *J Microsc* 111:219–223.
- Gurtin M. 1981. An introduction to continuum mechanics. Orlando: Academic Press.
- Hamilton P. 1993. A language to describe the growth of neurites. *Biol Cybern* 68:559–565.
- Haug H. 1984. Macroscopic and microscopic morphometry of the human brain and cortex. A survey in the light of new results. *Brain Pathol* 1:123–149.
- James J, Tanke HJ. 1991. Biomedical light microscopy. Dordrecht: Kluwer Academic Publishers.
- Koh W. 2000. Distributed, web-based microstructure database for brain tissue. Master of Science, Texas A & M University, College Station, TX.
- Landau LD, Lifshitz E. 1959. Theory of elasticity. London: Pergamon Press.
- Liljas A. 1999. Function is structure. *Science* 285:2077–2078.
- McCormick B. 2002. Technical report, Brain Networks Laboratory, Department of Computer Science, Texas AM University, College Station, TX.
- Merker B. 1983. Silver staining of cell bodies by means of physical development. *J Neurosci Methods* 9:235–241.
- Miller M, Christensen G, Amit Y, Grenander U. 1993. Mathematical textbook of deformable neuroanatomies. *Proc Natl Acad Sci USA* 90:11944–11948.
- Mitchison G. 1991. Neuronal branching patterns and the economy of cortical wiring. *Proc R Soc Lond B* 245:151–158.
- Modersitzki J. 2004. Numerical methods for image registration. Oxford: Oxford Science Publications.
- Modersitzki J, Schmitt O. 2001. Effiziente, nicht-lineare Registrierung eines histologischen Serienschchnittes durch das menschliche Gehirn. Workshop Bildverarbeitung in der Medizin (BVM 2001), Proceedings: Informatik aktuell. p 179–183.
- Modersitzki J, Obelöer W, Schmitt O, Lustig G. 1999. Elastic matching of very large scale digital images on high performance clusters. *LNCS* 1593:141–149.
- Murre J, Sturdy D. 1995. The connectivity of the brain: multi-level quantities analysis. *Biol Cybern* 73:529–545.
- Pakura M, Schmitt O, Aach T. 2002. Segmentation and analysis of nerve fibers in histologic sections of the cerebral human cortex. Proc. 5th IEEE Southwest Symposium on Image Analysis and Interpretation. Santa Fe 1:62–66.
- Ravasz E, Somera A, Mongru D, Oltvai Z, Barabási A.-L. 2002. Hierarchical organization of modularity in metabolic networks. *Science* 297:1551–1555.
- Rist S. 1999. Ein Ansatz zur Klassifizierung biologischer Neuronen mittels künstlicher neuronaler Netze. Institute of Mathematics, Medical University Lübeck, Germany. p 99–106.
- Roland PE, Zilles K. 1994. Brain atlases: a new research tool. *TINS* 17:458–467.
- Roland PE, Graufelds CJ, Wahlin J, Ingelman L, Andersson M, Ledberg A, Pedersen J, Akerman S, Dabringhaus A, Zilles K. 1994. Human brain atlas: for high resolution functional and anatomical mapping. *Hum Brain Map* 1:173–184.
- Romeis B. 1989. Mikroskopische technik. Urban und Schwarzenberg. München, Wien, Baltimore.
- Schleicher A, Amunts K, Geyer S, Kowalski T, Schormann T, Palomero-Gallagher N, Zilles K. 2000. A stereological approach to human cortical architecture: identification and delineation of cortical areas. *J Chem Neuroanat* 20:31–47.
- Schmitt O, Böhme M. 2002. A robust transcortical profile scanner for generating 2D-traverses in histological sections of rich curved cortical courses. *NeuroImage* 16:1103–1119.
- Schmitt O, Eggers R. 1997a. High contrast and homogeneous staining of paraffin sections of whole human brains for three dimensional ultrahigh resolution image analysis. *Biotech Histochem* 73:44–51.
- Schmitt O, Eggers R. 1997b. Systematic investigations of the contrast results of histochemical stainings of neurons and glial cells in the human brain by means of image analysis. *Micron* 28:197–215.
- Schmitt O, Eggers R. 1999. Flat-bed scanning as a tool for quantitative neuroimaging. *J Microsc* 196:337–346.
- Schmitt O, Modersitzki J, Obelöer W. 1999. The human neuroscanning project. *Neuroimage* 9:S22.
- Schmitt O, Hömke L, Dümbgen L. 2003. Detection of cortical transition regions utilizing statistical analyses of excess masses. *NeuroImage* 19:42–63.
- Schmolke C. 1996. Tissue compartments in laminae II-V of rabbit visual cortex - Three-dimensional arrangement, size and developmental changes. *Anat Embryol* 193:15–33.
- Schormann T, Zilles K. 1997. Limitations of the principal axes theory. *IEEE Trans Med Imag* 16:942–947.
- Schormann T, Zilles K. 1998. Three-dimensional linear and nonlinear transformations: an integration of light microscopical and MRI data. *Hum Brain Mapp* 6:339–347.
- Schormann T, Henn S, Zilles K. 1996. A new approach to fast elastic alignment with applications to human brains. *Lect Notes Comput Sci* 1131:337–342.
- Schwartz E. 1980. Computational anatomy and functional architecture of striate cortex: a spatial mapping approach to perceptual coding. *Vis Res* 20:645–669.
- Senft SL, Ascoli GA. 1999. Reconstruction of brain networks by algorithmic amplification of morphometry data. *LNCS* 1606:25–33.
- Skoglund T, Pascher R, Berthold C-H, Rydmark M, Jansson T, Gustavsson T. 1993. 3D reconstruction of biological objects from sequential image planes - applied on cerebral cortex from cat. *Comp Med Imag Graph* 17:165–174.
- Skoglund T, Pascher R, Berthold C-H. 1996. Aspects of the quantitative analysis of neurons in the cerebral cortex. *J Neurosci Methods* 70:201–210.
- Strogatz SH. 2001. Exploring complex networks. *Nature* 410:268–276.
- Sutoo D, Akiyama K, Yabe K. 1998. Quantitative mapping analyzer for determining the distribution of neurochemicals in the human brain. *J Neurosci Methods* 85:161–173.
- Talairach J, Tournoux P. 1993. Co-planar stereotactic atlas of the human brain: 3-dimensional proportional system: an approach to cerebral imaging. Thieme, Stuttgart.
- Toga AW, Ambach K, Quinn B, Hutchin M, Burton JS. 1994. Postmortem anatomy from cryosectioned whole human brain. *J Neurosci Methods* 54:239–252.
- von Economo C, Koskinas GN. 1925. Die Cytoarchitektonik der Hirnrinde des erwachsenen Menschen. Berlin: Springer.
- Young MP. 1992. Objective analysis of the topological organization of the primate cortical visual system. *Nature* 358:152–155.
- Young MP. 1996. The analysis of cortical connectivity. New York: Springer.